Earthquake Engineering & Structural Dynamics
The Journal of the International Association for Earthquake Engineering

EARTHQUAKE ENGINEERING & STRUCTURAL DYNAMICS
Earthquake Engng Struct. Dyn. (2016)
Published online in Wiley Online Library (wileyonlinelibrary.com). DOI: 10.1002/eqe.2699

Seismic response analysis of an interacting curved bridge–train system under frequent earthquakes

Qing Zeng and Elias G. Dimitrakopoulos*,†

Department of Civil and Environmental Engineering, The Hong Kong University of Science and Technology, Clear Water Bay, Kowloon, Hong Kong

SUMMARY

This paper establishes a scheme for the seismic analysis of interacting vehicle–bridge systems. The focus is on (horizontally) curved continuous railway bridges and frequent earthquakes. Main features of the proposed scheme are (i) the treatment of the dynamics in all three dimensions (3D), employing an additional rotating system of reference to describe the dynamics of the vehicles and a realistic 3D bridge model; (ii) the simulation of the creep interaction forces generated by the rolling contact between the wheel and the rail; and (iii) the integration of the proposed scheme with powerful commercial finite element software, during the pre-processing and post-processing phases of the analysis. The study brings forward the dynamics of a realistic vehicle–bridge (interacting) system during seismic shaking. For the (vehicle–bridge) case examined, the results verify the favorable damping effect the running vehicles have on the vibration of the deck. By contrast, the study stresses the adverse influence of the earthquake-induced bridge vibration on the riding comfort but, more importantly, on the safety of the running vehicles. In this context, the paper unveils also a vehicle–bridge–earthquake timing problem, behind the most critical vehicle response, and underlines the need for a probabilistic treatment. Among the 20 sets of historic records examined, the most crucial for the safety of the vehicles are near-fault ground motions. Finally, the study shows that even frequent earthquakes, of moderate intensity, can threaten the safety of vehicles running on bridges during the ground motion excitation, in accordance with recorded accidents.

Received 19 May 2015; Revised 7 December 2015; Accepted 7 December 2015

KEY WORDS: railway bridges; vehicle–bridge interaction; seismic response; curved bridges

1. INTRODUCTION

During the last 15 years, railway networks are expanding worldwide, and especially in Asia. Characteristically, contemporary high-speed railways (HSRs) use a high ratio of bridges. As a reference, from the 1318-km long Beijing–Shanghai HSR line in China, 1059 km is on (244) bridges, constituting 80.5% of the whole line [1]. Similarly, the total bridge length of the North-to-South Line from Taipei to Kaohsiung, in Taiwan, reaches 73% [1] of the whole line. With the length and the number of HSR bridges increasing, the possibility of train vehicles encountering an earthquake while crossing a bridge also increases [2]. Two alarming accidents (Figure 1) were already reported in the last 10 years. On October 23 2004, a train running at a speed of 200 km/h derailed during the Niigata-Chuetsu Earthquake with a magnitude of 6.8, near Niigata City, Japan, ending the 48-year safety record of the Shinkansen railway [3]. Six years later, on March 4, 2010 in southern Taiwan, a high-speed train derailed during the Jiashian earthquake with a magnitude of 6.4 and 53 km from the epicenter [4].

*Correspondence to: Elias G. Dimitrakopoulos, Department of Civil and Environmental Engineering, The Hong Kong University of Science and Technology, Clear Water Bay, Kowloon, Hong Kong.
†E-mail: ilias@ust.hk

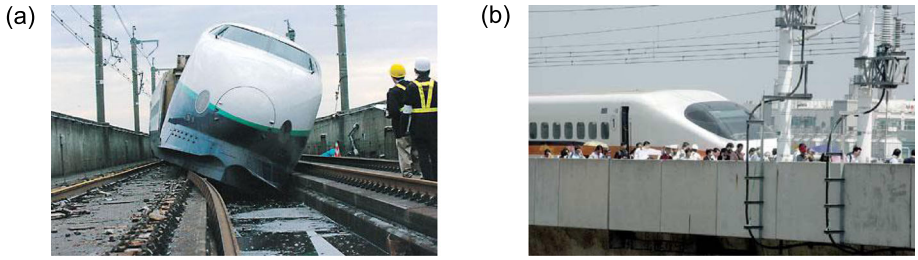

Figure 1. Derailment accidents of high-speed trains in (a) Japan [5] and in (b) Taiwan [6].

Given the potentially devastating consequences of similar future accidents, there is a growing need to shift the focus of analysis, and eventually design, from the seismic performance of the bridge structure, to the seismic performance of the interacting vehicle–bridge system. This is particularly true in light of the expanding railway bridges, the increasing operating speeds, and the strict safety requirements of conventional and HSR transportation [3]. This is an interdisciplinary research challenge, involving the treatment of the dynamics of the bridge structure (civil-earthquake engineering), together with the dynamics of the vehicle (mechanical engineering). Traditionally, the interaction with moving vehicles and the seismic shaking have been considered separately when analyzing the dynamics of bridges. Currently, there is a vast body of research on the seismic response of bridges separated from the running vehicles [7, 8], as well as on the dynamic vehicle–bridge interaction (VBI), without the consideration of earthquakes (e.g. [9] and references therein). By contrast, studies on the combined consideration of the effect of earthquakes on the interacting vehicle–bridge system are still scarce.

More specifically, Yang and Wu [10] investigated the stability of 3D train vehicle models, stationary or moving, on bridges shaken by earthquakes. They examined four sets of historical earthquake records scaled to a peak ground acceleration of 0.08 g. They concluded that, for the examined ground motions and bridge, a train was safer when stationary. That study also stressed the importance of the vertical ground motion component on the stability of the vehicle. Kim *et al.* studied the seismic response of interacting vehicle–bridge systems under moderate earthquakes, for steel monorail bridges [11], and for highway viaducts [12]. They showed that it is not realistic to treat the train vehicle merely as additional mass, as suggested by most seismic codes worldwide, for example, [13]. The seismic response of the bridge was reduced [11, 12] when the dynamics of the vehicles were properly simulated. On the contrary, the seismic response of the bridge was amplified when the vehicles were treated as additional vertical masses. The conclusions of the more recent similar study of He *et al.* [14] are in agreement with those of [11, 12]. Tanabe *et al.* [15, 16] studied numerically the behavior of the Shinkansen trains and railway bridges during earthquakes and checked experimentally part of their results. They also proposed [17] a method to capture numerically the interaction between the wheel and the rail in both the pre-derailment state and the post-derailment state, during an earthquake. Ju [4] investigated the derailment of high-speed trains moving on multi-span simply supported bridges due to historical earthquake records acting in all three directions. Matsumoto *et al.* [18] studied the running safety of railway vehicles on bridges subjected to earthquakes using an in-house computer simulation software. That study considered both the nonlinearity of the primary and secondary suspensions of the vehicles and the hysteretic characteristics of the bridge. Xia *et al.* [3] examined spatially non-uniform seismic ground motions and argued that not considering the seismic wave propagation effect leads to unsafe results regarding the vehicle running safety during earthquakes. Du *et al.* [19] extended the study of Xia *et al.* [3], taking into account the possible separations and recontact between the wheel and the rail. The results indicated that the wheel–rail separation time duration increased as the train speed increased, under non-uniform seismic ground motions. The analytical study of Yau and Fryba [20, 21] focused on the vibration of a suspension bridge due to a series of equidistant, identical moving loads, and under the propagation effect of the seismic waves in the vertical direction. That study concluded that the contribution of the higher modes on the peak acceleration of a long-span suspension bridge is significant and needs to be taken into consideration. Further, Yau [22] investigated the dynamic interaction of maglev trains moving over a suspension bridge under horizontal ground motions and stressed the

DOI: 10.1002/eqe

importance of the wave propagation effect on the dynamic response of the maglev vehicles. Zhang *et al.* [23] examined the seismic non-stationary random response of 3D train–bridge systems. Recently, Montenegro *et al.* [24] studied the dynamic stability of trains moving over bridges subjected to seismic excitations. Further, Montenegro *et al.* [25] proposed a wheel–rail contact model for analyzing the nonlinear lateral train–structure interaction. The model was verified with experiments performed on a rolling stock plant simulating track deviations caused by earthquakes.

This research is motivated by the need to elucidate the VBI dynamics between trains and railway bridges, during seismic excitation. The focus is on horizontally curved railway bridges. Recently, the authors proposed an analysis approach capable of tackling the VBI problem for curved (or straight) bridges and different types of vehicles [9]. That study [9] shed light on the VBI in curved bridges, but no seismic excitation was considered. Herein, the framework is extended in three ways: (i) the analysis considers a realistic bridge model; (ii) the interaction model simulates the creep forces generated by the rolling contact; and (iii) the analysis scheme is extended to account for the seismic ground motion excitation. The proposed approach covers also the (simpler) case of straight bridges and different types of vehicles.

2. PROPOSED ANALYSIS OF INTERACTING VEHICLE–BRIDGE SYSTEMS

Vehicle–bridge interaction refers to the coupling between the dynamic response of the vehicle and the supporting bridge: the vehicular loading on the bridge, causes the simultaneous vibration of the bridge, which in turn, acts as excitation for the vehicles. In general, the analysis of the VBI problem can be broken down to three main tasks: (i) the bridge modeling; (ii) the simulation of the vehicles and their motion; and (iii) the treatment of the interaction forces [26]. Sections (2.1) to (2.3) discuss the three tasks one by one.

2.1. Modeling of the bridge

The reference (hypothetical) bridge of this study is a horizontally curved, two-way (double-line), railway bridge (Figure 2). The bridge deck is a continuous prestressed concrete box girder with a total length of 207 m (Figure 2), which consists of five spans (36 + 45 × 3 + 36 m) and a radius of curvature $R = 750$ m. The section properties of the box girder are the torsional constant $I_p = 48.81$ m^4, the moment of inertia $I_{yy} = 29.87$ m^4, and $I_{zz} = 205.66$ m^4 accordingly and the cross-sectional area $A = 13.2$ m^2. The section of the reinforced concrete piers is a single-cell rectangular hollow section with a constant thickness of 0.5 m and a constant height of 6 m along the transverse direction. Along the longitudinal direction, the piers have a tapered section width (Figure 2(a)). At the top, the width of the piers is 4.0 m, whereas the section widths at the pier bottom are 4.38, 4.79, 4.75, and 4.27 m, respectively. The effective (reduced) flexural stiffness of the piers and the effective torsional stiffness of the deck, due to the cracking of the concrete section during an earthquake, are taken half the uncracked stiffness (assuming solid sections) [27]. The focus herein is on frequent, low-acceleration amplitude, earthquake excitations that do not activate the isolation system (e.g. friction pendulum bearings) and

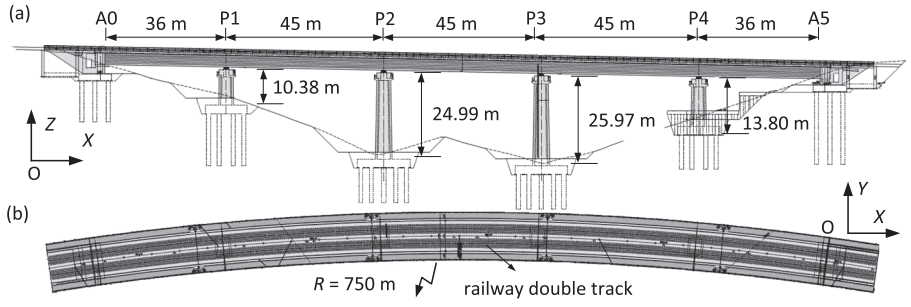

Figure 2. The curved two-way railway bridge examined: (a) elevation and (b) plan view.

DOI: 10.1002/eqe

do not force the bridge to behave inelastically/nonlinearly. Therefore, the study assumes a monolithic connection between the deck and the piers, and linear–elastic behavior of the bridge. For simplicity the analysis assumes the piers are fixed at their base.

For the scope of the VBI analysis, the two main choices for the numerical simulation of a bridge, are the finite element method (FEM) using the complete geometrical model [4, 9, 10, 28] and the modal superposition method [1–3, 15–22]. The present study adopts the former method (FEM). The finite element model of the bridge is built with ANSYS [29] software. The stiffness matrix $\mathbf{K}^B$, the mass matrix $\mathbf{M}^B$, and the Rayleigh damping matrix $\mathbf{C}^B$ are then exported to an in-house MATLAB [30] algorithm developed and verified, previously in [9]. Typical Euler–Bernoulli beam elements are utilized, and a damping ratio $\xi = 5\%$ [27] is assumed for the first two modes. The equation of motion (EOM) for the bridge is

$$\mathbf{M}^B\ddot{\mathbf{u}}^B + \mathbf{C}^B\dot{\mathbf{u}}^B + \mathbf{K}^B\mathbf{u}^B + \mathbf{W}_N^B\boldsymbol{\lambda}_N + \mathbf{W}_T^B\boldsymbol{\lambda}_T = \mathbf{F}^B \tag{1}$$

where, the superscript $()^B$ denotes the bridge system, $\mathbf{u}^B$ is the bridge displacement vector, and $\mathbf{F}^B$ is the vector of the loads acting on the bridge. When the seismic loading is considered, the force vector $\mathbf{F}^B$ is

$$\mathbf{F}^B = -{}_I\ddot{\mathbf{r}}_{OO^G}\boldsymbol{\delta}^B\mathbf{M}^B \tag{2}$$

where ${}_I\ddot{\mathbf{r}}_{OO^G}$ is the ground acceleration (Figure 5) at the base of the bridge and $\boldsymbol{\delta}^B$ is a unit vector connecting the components of the earthquake excitation to the pertinent degrees of freedom (DOFs) of the bridge. Following the standard convention, throughout this paper, the upper-dot denotes time differentiation. In Eq. (1), $\boldsymbol{\lambda}_N$ and $\boldsymbol{\lambda}_T$ are the contact forces vectors (Sections 2.3.2 and 2.3.1, respectively), and $\mathbf{W}_N^B$ and $\mathbf{W}_T^B$ are the corresponding direction matrices containing linear shape functions for the axial and torsional DOFs, and cubic (Hermitian) shape functions for the flexural DOFs [28]. Figure 3 presents the results of the modal analysis of the bridge model. The results agree well with the pertinent results of [31].

2.2. *Simulation of the train vehicles and of the vehicle dynamics*

In most recent studies on vehicle–bridge interaction (e.g. [1–4, 9–12, 14–19]), the vehicle model is a multibody assembly. Similarly, herein, each train vehicle model (Figure 4) is composed of one car body, two bogies, and four wheelsets, connected with linear springs and viscous dashpots, representing the characteristics of the suspension system. All components are considered as rigid bodies, neglecting their elastic deformations. The car body and the bogies have six DOFs each, with acceleration vector $\ddot{\mathbf{u}}^u$

$$\ddot{\mathbf{u}}^u = \left[\ \ddot{s}^u \ \ \ddot{y}^u \ \ \ddot{z}^u \ \ \ddot{\psi}^u \ \ \ddot{\phi}^u \ \ \ddot{\theta}^u\ \right]^{\mathrm{T}} \tag{3}$$

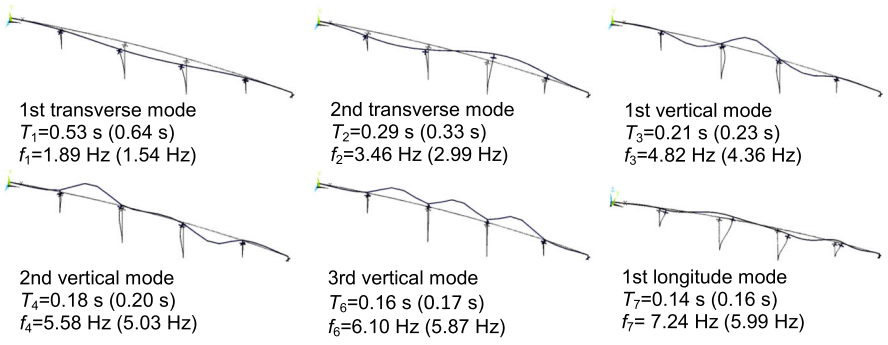

Figure 3. The first six modes of the bridge: the periods/frequencies outside (inside) the parentheses are based on the uncracked (effective) stiffness of the piers and the deck.

DOI: 10.1002/eqe

where the superscript 'T' denotes the transpose of a matrix throughout this paper. Each wheelset has five DOFs, with acceleration vector $\ddot{\mathbf{u}}^w$ (Figure 4):

$$\ddot{\mathbf{u}}^w = \left[\ddot{s}^w \quad \ddot{y}^w \quad \ddot{z}^w \quad \ddot{\psi}^w \quad \ddot{\phi}^w \right]^{\mathrm{T}} \tag{4}$$

where s, y, and z are the longitudinal, lateral, and vertical displacements, respectively; while ψ, ϕ, and θ are the yawing, rolling, and pitching Euler angle (Figure 4(d)), respectively. Overall each train vehicle has 38 DOFs.

The 3D seismic excitation activates the longitudinal DOFs of the vehicle (along the tangential sense of the bridge). The analysis, therefore, considers the longitudinal dynamics of the vehicles, which in the absence of the seismic excitation would be typically neglected; the train would run on the bridge at a constant speed. Further simulation assumptions for the train vehicles are (i) The study assumes that before the train enters the bridge, it travels on a rigid embankment with the same radius of curvature and the same track irregularities as on the bridge. Therefore, the vehicles enter the bridge with non-zero initial deformation: an approach similar to [32]. (ii) The train consists of a series of 10 identical train vehicles, each of which and its corresponding DOFs, are independent of the adjacent vehicles, similar to [2, 3]. This assumption is verified by checking the relative displacements between adjacent vehicles after the analysis. (iii) The train travels over the bridge with a constant speed (e.g [2, 3]), which is a limitation of the present approach for simplicity.

The simulation of the 3D dynamics of a vehicle traveling on a curved path is a challenging task. The employed approach stems from the framework introduced in [33]. Key feature of the approach is the use of a *moving trajectory system* TI. The trajectory system follows the vehicle along its curved trajectory, with its origin O^{ti} uniquely defined by the arc length s^i, and its longitudinal axis $O^{ti}X^{ti}$ set tangent to the curve, at the origin O^{ti} (Figure 5).

The Newton–Euler equations describe the motion of the vehicle in terms of generalized trajectory coordinates as [33]

$$\mathbf{M}^V \ddot{\mathbf{u}}^V = \mathbf{F}_e^V + \mathbf{F}_v^V \tag{5}$$

where $\mathbf{M}^V$ is the mass matrix, $\mathbf{F}_e^V$ is the external forces vector, $\mathbf{F}_v^V$ is the inertial forces vector (due to the curved path-rotating system of reference), and $\mathbf{u}^V \in \mathbb{R}^{38,1}$ is the generalized displacement vector of the vehicle, in the *moving trajectory system*. The nomenclature $\in \mathbb{R}^{38,1}$ denotes a real matrix with 38 rows and one column. The superscript $()^V$ stands for the vehicle subsystem.

To illustrate the details of Eq. (5), consider a specific rigid body component of the vehicle, for instance, the car body of Figure 5 (indicated with a superscript i). The vector ${}_I\ddot{\mathbf{r}}^i_{OO^{ir}}$ of the linear

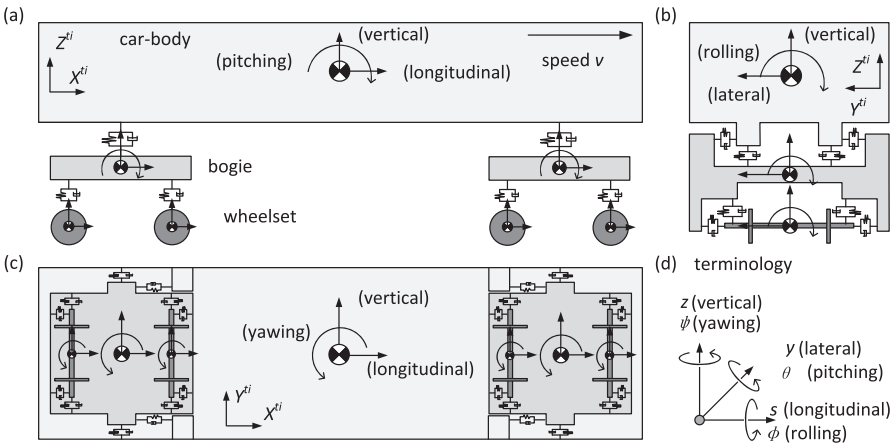

Figure 4. The vehicle model adopted: (a) side view, (b) back view, (c) top view, and (d) coordinate system, with the arrows indicating the degrees of freedom.

DOI: 10.1002/eqe

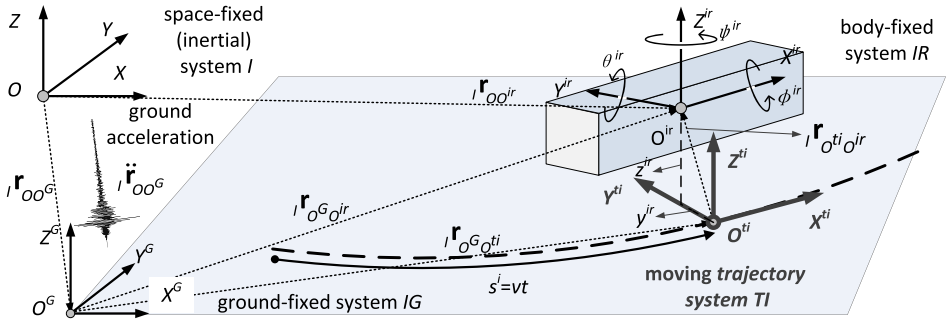

Figure 5. The four coordinate systems employed to describe the dynamics of the vehicle during earthquake excitation.

(translational) accelerations of the center of mass, of the rigid body, in the space-fixed system is (Figure 5)

$$ {}_I\ddot{\mathbf{r}}^i_{OO^{ir}} = {}_I\ddot{\mathbf{r}}_{OO^G} + {}_I\mathbf{L}^i{}_{TI}\ddot{\mathbf{u}}^i + {}_I\boldsymbol{\gamma}^i_R \tag{6} $$

where ${}_I\ddot{\mathbf{r}}_{OO^G}$ is the ground acceleration vector (Figure 5). Throughout this paper, left-subscripts declare the coordinate system (Figure 5) each vector/matrix is referring to. Assuming that the seismic ground motion is purely translational, the absolute angular acceleration of the rigid body ${}_{IR}\boldsymbol{\alpha}^i$, in the body-fixed system, is

$$ {}_{IR}\boldsymbol{\alpha}^i = {}_{IR}\mathbf{H}^i{}_{TI}\ddot{\mathbf{u}}^i + {}_{IR}\boldsymbol{\gamma}^i_\alpha \tag{7} $$

Matrices ${}_I\mathbf{L}^i(t)$ and ${}_{IR}\mathbf{H}^i(t)$ arise because of the curvature of the path (rotating reference system). They are time-varying velocity transformation matrices pertaining to the translational, and the rotational, DOFs, respectively [33]. Vectors ${}_I\boldsymbol{\gamma}^i_R$ and ${}_{IR}\boldsymbol{\gamma}^i_\alpha$ contain the additional quadratic velocity terms, produced during the time differentiation of the absolute linear, and absolute angular velocities, respectively [33].

The mass matrix of the rigid body i is [33]

$$ \mathbf{M}^i(t) = {}_I\mathbf{L}^i(t)^{\mathrm{T}} m^i {}_I\mathbf{L}^i(t) + {}_{IR}\mathbf{H}^i(t)^{\mathrm{T}}{}_{IR}\mathbf{I}^i_{\theta\theta}{}_{IR}\mathbf{H}^i(t) \tag{8} $$

where m^i is the mass and ${}_{IR}\mathbf{I}^i_{\theta\theta}$ is the inertia tensor about the principal axes of the rigid body i. Particularly, for a single rigid body i, the seismic loading vector $\mathbf{F}^i_G$ (when considered) is

$$ \mathbf{F}^i_G = -m^i {}_I\mathbf{L}^i(t)^{\mathrm{T}}{}_I\ddot{\mathbf{r}}_{OO^G} \tag{9} $$

The inertial forces vector (due to the curvature of the path) is

$$ \mathbf{F}^i_v = -m^i {}_I\mathbf{L}^i(t)^{\mathrm{T}}{}_I\boldsymbol{\gamma}^i_R - {}_{IR}\mathbf{H}^i(t)^{\mathrm{T}}\left({}_{IR}\mathbf{I}^i_{\theta\theta}{}_{IR}\boldsymbol{\gamma}^i_\alpha + {}_{IR}\boldsymbol{\omega}^i \times \left({}_{IR}\mathbf{I}^i_{\theta\theta}{}_{IR}\boldsymbol{\omega}^i\right)\right) \tag{10} $$

where the centrifugal forces and the Coriolis forces arise because of the curvature of the vehicle's path and ${}_{IR}\boldsymbol{\alpha}^i$ is the angular velocity vector defined in the body-fixed system.

The EOM (5) for the vehicle subsystem (Figure 4) takes the form:

$$ \mathbf{M}^V\ddot{\mathbf{u}}^V + \mathbf{C}^V\dot{\mathbf{u}}^V + \mathbf{K}^V\mathbf{u}^V - \mathbf{W}^V_N\boldsymbol{\lambda}_N - \mathbf{W}^V_T\boldsymbol{\lambda}_T = \mathbf{F}^V \tag{11} $$

DOI: 10.1002/eqe

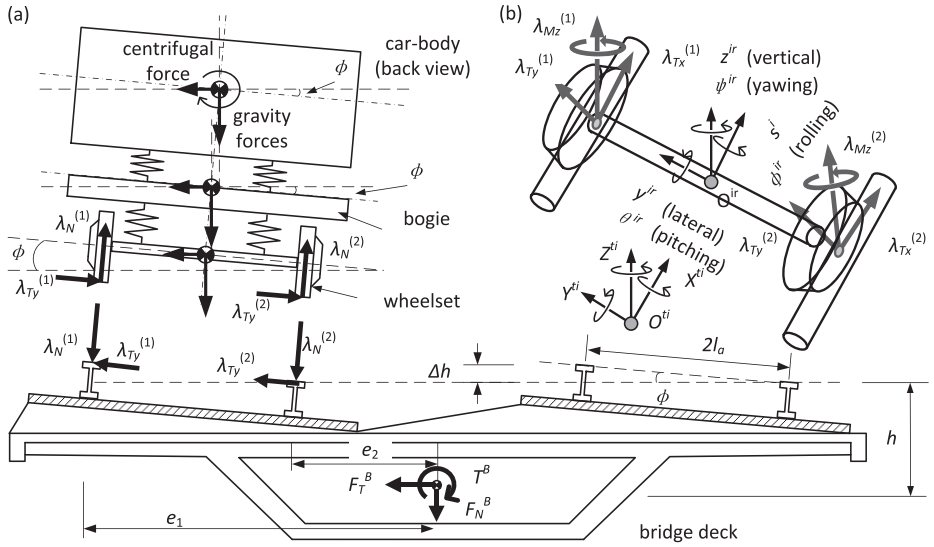

Figure 6. (a) The contact forces of the vehicle–bridge system and (b) creep forces of one single wheelset.

where $\mathbf{M}^V$, $\mathbf{K}^V$, and $\mathbf{C}^V$ are the mass matrix, the stiffness matrix, and the damping matrix of the vehicle system. For all cases examined in this study (Section 3), the details of $\mathbf{K}^V$ and $\mathbf{C}^V$ for the vehicle in Figure 4 are given in Ref. [34]. The time-dependent mass matrix $\mathbf{M}^V(t)$ is derived using Eq. (8). Figure 6 shows the normal contact forces $\boldsymbol{\lambda}_N$ and the creep forces $\boldsymbol{\lambda}_T$ (Sections 2.3.2 and 2.3.1). $\mathbf{W}_N^V$ and $\mathbf{W}_T^V$ are the corresponding pertinent contact direction matrices, where the subscripts N and T stand for the normal and the tangential directions of contact throughout this paper (see, e.g., Pfeiffer and Glocker [35]).

2.3. *Global equations of motion and interaction model*

One way to derive the EOMs of the coupled vehicle–bridge system is by gathering the two subsystems into a single one (e.g. [3,9–12,19]). Following this approach, the EOM's of the coupled vehicle–bridge system can be written as

$$\mathbf{M}^*\ddot{\mathbf{u}} + \mathbf{C}\dot{\mathbf{u}} + \mathbf{K}\mathbf{u} - \mathbf{W}_N\boldsymbol{\lambda}_N - \mathbf{W}_T\boldsymbol{\lambda}_T = \mathbf{F} \tag{12}$$

where the global displacement vector $\mathbf{u}$, the global mass $\mathbf{M}^*$, stiffness $\mathbf{K}$ and damping $\mathbf{C}$ matrix, and the global force vector $\mathbf{F}$ are created by assembling the pertinent matrices of the two individual subsystems as

$$\mathbf{u} = \begin{bmatrix} \mathbf{u}^V \\ \mathbf{u}^B \end{bmatrix},\ \mathbf{M}^* = \begin{bmatrix} \mathbf{M}^V & \mathbf{0} \\ \mathbf{0} & \mathbf{M}^B \end{bmatrix},\ \mathbf{C} = \begin{bmatrix} \mathbf{C}^V & \mathbf{0} \\ \mathbf{0} & \mathbf{C}^B \end{bmatrix},\ \mathbf{K} = \begin{bmatrix} \mathbf{K}^V & \mathbf{0} \\ \mathbf{0} & \mathbf{K}^B \end{bmatrix},\ \mathbf{F} = \begin{bmatrix} \mathbf{F}^V \\ \mathbf{F}^B \end{bmatrix} \tag{13}$$

The symbol $()^*$ indicates that the mass matrix is time dependent. $\boldsymbol{\lambda}_N$ contains the normal contact forces discussed in Section 2.3.2, and $\boldsymbol{\lambda}_T$ is the creep forces vector:

$$\boldsymbol{\lambda}_T = \begin{bmatrix} \boldsymbol{\lambda}_{Tx} & \boldsymbol{\lambda}_{Ty} & \boldsymbol{\lambda}_{Mz} \end{bmatrix}^{\mathrm{T}} \tag{14}$$

where $\boldsymbol{\lambda}_{Tx}$ is the longitudinal creep force, $\boldsymbol{\lambda}_{Ty}$ is the lateral creep force, and $\boldsymbol{\lambda}_{Mz}$ is the spin creep moment vector (Figure 6(b)), calculated according to Section 2.3.1. The global direction matrices $\mathbf{W}_N$, $\mathbf{W}_T$ can be broken down to

$$\mathbf{W}_N = \begin{bmatrix} \mathbf{W}_N^V \\ -\mathbf{W}_N^B \end{bmatrix}, \mathbf{W}_T = \begin{bmatrix} \mathbf{W}_T^V \\ -\mathbf{W}_T^B \end{bmatrix} = \begin{bmatrix} \begin{bmatrix} \mathbf{W}_{Tx}^V & \mathbf{W}_{Ty}^V & \mathbf{W}_{Mz}^V \end{bmatrix} \\ -\begin{bmatrix} \mathbf{W}_{Tx}^B & \mathbf{W}_{Ty}^B & \mathbf{W}_{Mz}^B \end{bmatrix} \end{bmatrix} \tag{15}$$

DOI: 10.1002/eqe

with submatrices $\mathbf{W}_{Tx}$, $\mathbf{W}_{Ty}$, and $\mathbf{W}_{Mz}$ (of each subsystem) corresponding, to the directions of $\boldsymbol{\lambda}_{Tx}$, $\boldsymbol{\lambda}_{Ty}$, and $\boldsymbol{\lambda}_{Mz}$, respectively. The study takes into account the track cant angle and the offsets of the track (Figure 6(a)) as in [9]. The only non-zero entries in the contact direction matrices $\mathbf{W}$ are, at each given time, those associated with the DOFs participating in the contact, and they change in time as a function of the contact point location s^i [9]. While the train passes over the bridge, the contact forces change with respect to both time (t) and space (s^i). The contact forces λ_N and λ_T between the wheels and the bridge (Figure 6) couple the two sets of equations, Eqs. (1) and (11), describing the response of the two subsystems. A key point of the VBI problem is the treatment of the coupling contact forces. This study calculates the contact forces along the normal direction and the tangential direction differently.

2.3.1. Tangential contact forces – creep force model. The rolling contact between the wheel and the rail generates creep forces and moments (Figure 6(b)). To account for the high creepage during earthquakes, the creep force model adopted (Shen–Hedrick–Euristic modification [36]) considers the nonlinear relationship between the creepage and the creep forces. The calculation of the lateral flange contact forces follows the model in [37]. To demonstrate the calculation procedure, consider a single wheel of the wheelset (denoted with the superscript i) of the vehicle model (Figure 6(b)). The longitudinal creep forces ${\lambda_{Tx}}^i$, the lateral creep forces ${\lambda_{Ty}}^i$, and the spin creep moments ${\lambda_{Mz}}^i$ are connected with the corresponding longitudinal creepage ${\xi_x}^i$, the lateral creepage ${\xi_y}^i$, and the spin creepage ${\xi_\psi}^i$:

$$ {\boldsymbol{\lambda}_T}^i = {\mathbf{f}_T}^i {\boldsymbol{\xi}_T}^i \tag{16} $$

where ${\boldsymbol{\lambda}_T}^i$ is as in Equation (14), and similarly

$$ {\boldsymbol{\xi}_T}^i = \left[{\xi_x}^i \;\; {\xi_y}^i \;\; {\xi_\psi}^i \right]^{\mathrm{T}} \tag{17} $$

while ${\mathbf{f}_T}^i$ is a creep coefficient matrix, defined as

$$ {\mathbf{f}_T}^i = \varepsilon^i \begin{bmatrix} -f_{33} & 0 & 0 \\ 0 & -f_{11} & -f_{12} \\ 0 & f_{12} & -f_{22} \end{bmatrix} \tag{18} $$

f_{11}, f_{12}, f_{22}, and f_{33} are the pertinent Kalker's creep coefficients [36]. The saturation constant ε^i is calculated based on the creep forces [36]

$$ \varepsilon^i = \begin{cases} \frac{1}{\beta^i}\left[\beta^i - \frac{1}{3}{\beta^i}^2 + \frac{1}{27}{\beta^i}^3\right] & for\ \beta^i \le 3 \\ \frac{1}{\beta^i} & for\ \beta^i > 3 \end{cases} \tag{19} $$

where

$$ \beta^i = \frac{\sqrt{\left({\lambda_{Tx}}^i\right)^2 + \left({\lambda_{Ty}}^i\right)^2}}{\mu {\lambda_N}^i} \tag{20} $$

μ is the coefficient of friction and ${\lambda_N}^i$ is the normal contact force. The creepage vector contains the normalized relative velocity between the wheel and the rail and can be written as

$$ {\boldsymbol{\xi}_T}^i = \frac{1}{\dot{s}^i}\left({\mathbf{W}_T}^i\right)^{\mathrm{T}} \dot{\mathbf{p}}^{wi} \tag{21} $$

DOI: 10.1002/eqe

where

$$\mathbf{W}_T{}^i = \left[\mathbf{W}_{Tx}{}^i \;\; \mathbf{W}_{Ty}{}^i \;\; \mathbf{W}_{Mz}{}^i \right] \tag{22}$$

For the calculation of the creep forces, the generalized velocity vector of the wheelset $\dot{\mathbf{u}}^{wi}$ is augmented with the angular pitching velocity of the wheelset $\dot{\theta}^{wi} = \dot{s}^{wi}/r_w$, where r_w is the radius of the wheel

$$\dot{\mathbf{p}}^{wi} = \mathbf{A}^i \dot{\mathbf{u}}^{wi} + \mathbf{b}^i \dot{\theta}^{wi} \tag{23}$$

$\mathbf{A}^i$ and $\mathbf{b}^i$ are merely auxiliary matrices adjusting the dimensions of $\dot{\mathbf{u}}^{wi}$ (Eq. (11)) and $\dot{\theta}^{wi}$

$$\mathbf{A}^i = \begin{bmatrix} \mathbf{E} \in \mathbb{R}^{5,5} & \mathbf{0} \in \mathbb{R}^{5,1} \\ \mathbf{0} \in \mathbb{R}^{1,5} & 0 \end{bmatrix}, \; \mathbf{b}^i \in \begin{bmatrix} \mathbf{0} \in \mathbb{R}^{5,1} \\ 1 \end{bmatrix} \tag{24}$$

The creep force vector (16) becomes

$$\boldsymbol{\lambda}_T{}^i = \frac{1}{\dot{s}^{wi}} \mathbf{f}_T{}^i \left(\mathbf{W}_T{}^i\right)^{\mathrm{T}} \left(\mathbf{A}^i \dot{\mathbf{u}}^{wi} + \mathbf{b}^i \dot{\theta}^{wi}\right) \tag{25}$$

Substituting vector $\boldsymbol{\lambda}_T$ from Eq. (25) to Eq. (12), the EOM takes the form

$$\mathbf{M}^*(t)\,\ddot{\mathbf{u}}(t) + \left(\mathbf{C} + \mathbf{C}_\xi(t)\right)\dot{\mathbf{u}}(t) + \mathbf{K}\mathbf{u}(t) - \mathbf{W}_N(t)\,\boldsymbol{\lambda}_N(t) = \mathbf{F}(t) - \mathbf{F}_\xi(t) \tag{26}$$

where $\mathbf{C}_\xi$ and $\mathbf{F}_\xi$ is the equivalent damping matrix and force vector due to the creep forces, given as

$$\mathbf{C}_\xi = \frac{1}{\dot{s}^i}\mathbf{A}^{\mathrm{T}}\mathbf{W}_T\mathbf{f}_T\mathbf{W}_T{}^{\mathrm{T}}\mathbf{A}, \; \mathbf{F}_\xi = \frac{1}{\dot{s}^i}\mathbf{A}^{\mathrm{T}}\mathbf{W}_T\mathbf{f}_T\mathbf{W}_T{}^{\mathrm{T}}\mathbf{b}\dot{\theta}^{wi} \tag{27}$$

2.3.2. Normal contact forces – kinematical approach. To solve the global EOMs (26), the normal contact forces need to be calculated first. The basic assumption of the calculation is that the wheel is always in contact with the rail. This assumption implies that the relative distance between the wheel and the rail $\mathbf{g}_N$ is zero, that is, no separation between them occurs- a kinematic constraint. The relative normal distance or normal contact displacement is

$$\mathbf{g}_N = \mathbf{W}_N{}^{\mathrm{T}}\mathbf{u} + \mathbf{r}_{cN} = \mathbf{0} \tag{28}$$

where $\mathbf{r}_{cN}$ represents the track elevation irregularities [28]. The track irregularities are simulated as a stationary stochastic process using the *spectral representation method* [28] and the German track spectra [1]. On the acceleration level, the kinematical constraint of Eq. (28) becomes

$$\ddot{\mathbf{g}}_N = \mathbf{0} \tag{29}$$

Differentiation of Eq. (28), with respect to time, gives the pertinent contact velocity

$$\dot{\mathbf{g}}_N = \frac{\mathrm{d}}{\mathrm{d}t}\left(\mathbf{W}_N{}^{\mathrm{T}}\mathbf{u} + \mathbf{r}_{cN}\right) = \mathbf{W}_N{}^{\mathrm{T}}\dot{\mathbf{u}} + \tilde{\mathbf{w}}_N \tag{30}$$

DOI: 10.1002/eqe

and the contact acceleration

$$\ddot{\mathbf{g}}_N = \frac{\mathrm{d}^2}{\mathrm{d}t^2}\left(\mathbf{W}_N{}^{\mathrm{T}}\mathbf{u} + \mathbf{r}_{cN}\right) = \mathbf{W}_N{}^{\mathrm{T}}\ddot{\mathbf{u}} + \bar{\mathbf{w}}_N \tag{31}$$

where $()'$ stands for differentiation with respect to the space s^i and vectors $\tilde{\mathbf{w}}_N$ and $\bar{\mathbf{w}}_N$ (Eq. (30)) contain the redundant terms of the time differentiations

$$\begin{aligned} \tilde{\mathbf{w}}_N &= v\mathbf{W}'_N{}^{\mathrm{T}}\mathbf{u} + v\mathbf{r}'_{cN} \\ \bar{\mathbf{w}}_N &= 2v\mathbf{W}'_N{}^{\mathrm{T}}\dot{\mathbf{u}} + v^2\mathbf{W}''_N{}^{\mathrm{T}}\mathbf{u} + v^2\mathbf{r}''_{cN} \end{aligned} \tag{32}$$

Solving the EOM (26) for $\ddot{\mathbf{u}}$ and substituting into Eq. (30) returns

$$\ddot{\mathbf{g}}_N = \mathbf{W}_N{}^{\mathrm{T}}\mathbf{M}^*(t)^{-1}\mathbf{h} + \mathbf{G}_{NN}\boldsymbol{\lambda}_N + \bar{\mathbf{w}}_N \tag{33}$$

where $\mathbf{G}_{NN} = \mathbf{W}_N{}^{\mathrm{T}}\mathbf{M}^*(t)^{-1}\mathbf{W}_N$ and the $\mathbf{h}$ vector is equal to

$$\mathbf{h} = \left(\mathbf{F} - \mathbf{F}_\xi\right) - \left(\mathbf{C} + \mathbf{C}_\xi\right)\dot{\mathbf{u}} - \mathbf{K}\mathbf{u} \tag{34}$$

The normal contact forces $\boldsymbol{\lambda}_N$ can now be derived from Eq. (33) with the help of Eq. (29):

$$\boldsymbol{\lambda}_N = -\mathbf{G}_{NN}{}^{-1}\left(\mathbf{W}_N{}^{\mathrm{T}}\mathbf{M}^*(t)^{-1}\mathbf{h} + \bar{\mathbf{w}}_N\right) \tag{35}$$

Substituting Eq. (35) into the EOM (26) and regrouping yields the EOM for the coupled bridge–vehicle system:

$$\mathbf{M}^*(t)\,\ddot{\mathbf{u}}(t) + \mathbf{C}^*(t)\,\dot{\mathbf{u}}(t) + \mathbf{K}^*(t)\,\mathbf{u}(t) = \mathbf{F}^*(t) \tag{36}$$

with

$$\begin{cases} \mathbf{C}^*(t) = \left[\mathbf{E} - \mathbf{W}_N(t)\,\mathbf{G}_{NN}^{-1}(t)\,\mathbf{W}_N{}^{\mathrm{T}}(t)\,\mathbf{M}^{*-1}(t)\right]\left(\mathbf{C} + \mathbf{C}_\xi(t)\right) + 2v\mathbf{W}_N(t)\,\mathbf{G}_{NN}^{-1}(t)\,\mathbf{W}''_N{}^{\mathrm{T}}(t) \\ \mathbf{K}^*(t) = \left[\mathbf{E} - \mathbf{W}_N(t)\,\mathbf{G}_{NN}^{-1}(t)\,\mathbf{W}_N{}^{\mathrm{T}}(t)\,\mathbf{M}^{*-1}(t)\right]\mathbf{K} + v^2\mathbf{W}_N(t)\,\mathbf{G}_{NN}^{-1}(t)\,\mathbf{W}'_N{}^{\mathrm{T}}(t) \\ \mathbf{F}^*(t) = \left[\mathbf{E} - \mathbf{W}_N(t)\,\mathbf{G}_{NN}^{-1}(t)\,\mathbf{W}_N{}^{\mathrm{T}}(t)\,\mathbf{M}^{*-1}(t)\right]\left(\mathbf{F}(t) - \mathbf{F}_\xi(t)\right) - v^2\mathbf{W}_N(t)\,\mathbf{G}_{NN}^{-1}(t)\,\mathbf{r}''_{cN} \end{cases} \tag{37}$$

where $\mathbf{E}$ is a unit matrix and v the velocity of the vehicle. The stiffness matrix, the damping matrix, and the loading vector of the whole system become time dependent. In addition, the global mass matrix is also time dependent because of the curvature of the vehicle's path. The EOMs (36) and (37) are numerically integrated in a state-space form with the aid of the available in MATLAB ordinary differential equation solvers for large, stiff systems [30, 38] verified previously [9]. The integration scheme is of variable order, and it is based on the numerical differentiation formulas [38]. The adopted absolute tolerance is 10^{-4}. For the post-processing of the response (visualization of the results), and not for the analysis of the response, this study employs again the commercially available software ANSYS [29].

DOI: 10.1002/eqe

3. RESULTS AND DISCUSSION

This section examines and compares the following three different scenarios: the dynamic interaction between moving train vehicles and a railway bridge, in the absence of earthquakes (Section 3.1); the seismic response of the bridge not considering the dynamics of the vehicles (conventional approach in earthquake engineering, Section 3.2); and the seismic response of a VBI system (proposed model, Section 3.3).

3.1. Dynamic vehicle–bridge interaction analysis

The dynamic VBI starts when the first vehicle enters the bridge and stops when the last vehicle of the train leaves the bridge. After a vehicle leaves the bridge, its response is no longer of interest for this study. The speed of the vehicle is 120 km/h (33.33 m/s), and the track cant angle (Figure 6) is $\phi = 0.105$. The conicity of the wheels is 0.05, and the rails have a knife-edge shape, as in [37]. The train consists of 10 identical vehicles, with the properties given in [34]. Because of the curvature of the bridge/rail, the VBI triggers the response in the vertical, the radial (horizontal), and the torsional senses of the bridge. The excitation stems not only from the track irregularities and the wheel hunting due to creep but also from the centrifugal and the coriolis forces. The present section does not account for external loading (e.g. earthquake excitation or wind loading). To compare the response of the bridge from the present VBI analysis with the seismic response of the interacting vehicle–bridge system in Section 3.3, this section considers both the uncracked stiffness and the effective stiffness of the piers and the deck.

Figure 7 plots the time histories of the midpoint displacement of the bridge (u^{Bv} and u^{Br}), together with the accelerations of the car body of the first vehicle (a^{Vv} and a^{Vr}). In the absence of earthquakes, the accelerations of the later vehicles (from the second to the tenth one) are similar with those of the first vehicle and therefore are omitted from Figure 7 for brevity. Under the passage of 10 identical vehicles, the bridge deflects mainly along the radial direction (Figure 7(b)) than along the vertical direction (Figure 7(a)). More importantly, the deformation patterns along the two directions of the bridge are different. Figure 8 captures the deformed shape of the whole bridge (elevation view and plan view) at different time instants, considering the effective stiffness of the piers and the deck. The three time instants in Figure 8 correspond to the time the first vehicle reaches the first pier, the midpoint of the middle span, and the end abutment, respectively. Consequently, running vehicles occupy solely the side span of the deck at $t = 1.1$ s, half of the deck at $t = 3.1$ s, and the entire length of the deck at $t = 6.2$ s. Along the vertical direction, the deck deflects as a continuous beam (Figure 8(a), (c), and (e)). Along the radial direction, the bridge behaves almost as a bridge/beam simply supported at

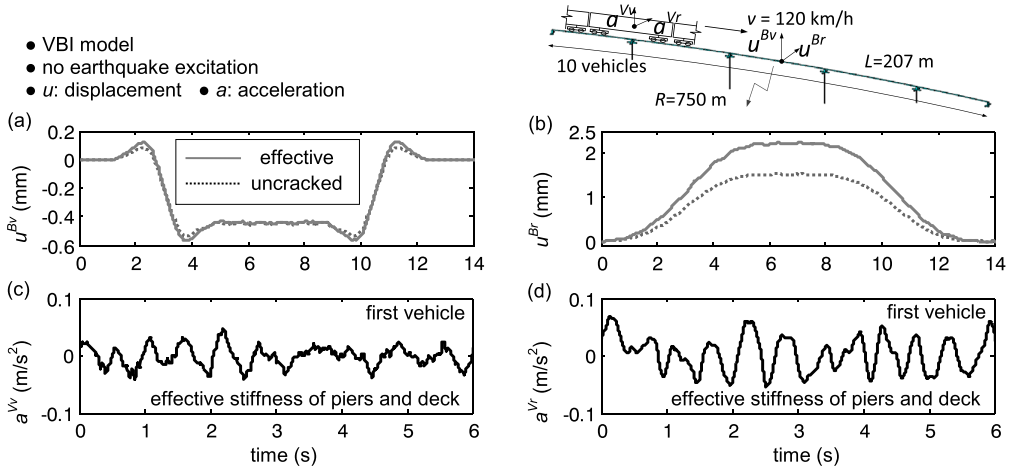

Figure 7. The dynamic vehicle–bridge interaction (VBI) induced by 10 identical moving vehicles: (a) the vertical and (b) the radial displacement time history of the midpoint of the bridge and (c) the vertical and (d) the radial acceleration time history of the car body of the vehicle.

DOI: 10.1002/eqe

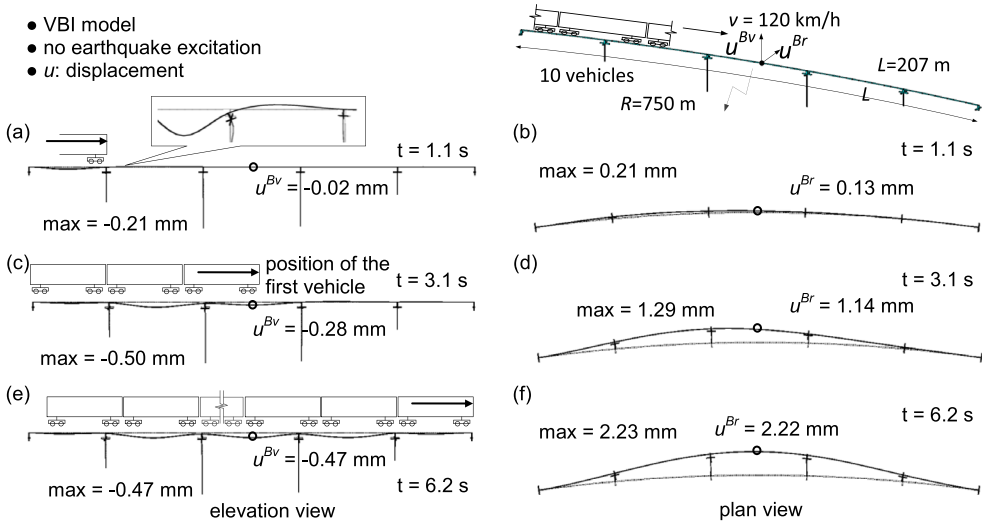

Figure 8. The deformed shape of the whole bridge induced by 10 identical moving vehicles: (a), (c), and (e) elevation view; (b), (d) and (f) plan view.

its end abutments (Figure 8(b), (d), and (f)). As a consequence, the lateral load on the deck builds up, almost monotonically, as the moving vehicles accumulate on the bridge (Figure 8(b), (d), and (f)), and accordingly varies the response displacement. In other words, in the lateral direction, the behavior of the bridge due to the VBI resembles quasi-static loading conditions. The magnitude of the peak vertical deflection (0.47 mm at $t = 6.2$ s) for the fully loaded deck is lower than that (0.50 mm at $t = 3.1$ s) for a half-loaded deck (Figure 8(c) and (e)), as expected from the influence lines for static loads. Recall though that the dynamic VBI is highly sensitive on the speed of the vehicle, which effectively defines a loading frequency. For a different vehicle speed, the response of the vehicle–bridge system might change dramatically [9].

The response of the vehicle is also of interest, in particular, with respect to its safety and comfort [9]. A critical quantity for the riding comfort of the passengers is the acceleration of the car body. Figure 7(c) and (d) plots the vertical and the radial accelerations of the car body of the first vehicle. As expected, the maximum accelerations are well below the contemporary code limits for conventional railway (e.g. [32]): 2.0 (for the vertical) and 1.5 $\mathrm{m/s^2}$ (for the radial acceleration). Two important metrics of the safety of the running vehicle are [32] the *derailment factor* and the *offload factor*. The derailment factor is the ratio of the lateral contact force and the vertical contact force acting on the same wheel. The offload factor is the ratio between the dynamic reduction of the vertical contact force (difference between the dynamic and the static values) and the static vertical contact force acting on the same wheel [32]. The allowable values for the derailment factor and the offload factor are 0.8 and 0.6, respectively (e.g. [32]). The calculated peak derailment factor and peak offload factor are 0.15 and 0.12, respectively. Thus, when no earthquake is considered, all aforementioned comfort and safety metrics for the vehicle are clearly satisfied.

3.2. Conventional seismic response analysis of the bridge

Herein, the focus is on frequent, and hence of low or moderate acceleration amplitude, earthquake excitations. As a sample, Figure 9 plots a historic ground motion recorded on July 15, 2012, in Nakagawa, Japan, during a 4.2-magnitude earthquake event [39]. Figure 9 shows the time histories of the three components of the ground acceleration: upper–down, north–south, and east–west , and their Fourier spectra. The study assumes that the upper–down component acts along the Z-vertical direction of the bridge system (Figure 2), the north–south component along the X-longitudinal direction, and the east–west component along the Y-lateral direction.

The conventional approach in seismic engineering (e.g. EC8 [27]) is to represent the traffic during an earthquake excitation as an additional quasi-permanent mass, which according to EC8 [27] for railway bridges is $\psi_{2,1}\mathrm{Q}_{\mathrm{k},1} = 0.3\mathrm{Q}_{\mathrm{k},1}$. Further, the seismic analysis of the bridge adopts the effective

DOI: 10.1002/eqe

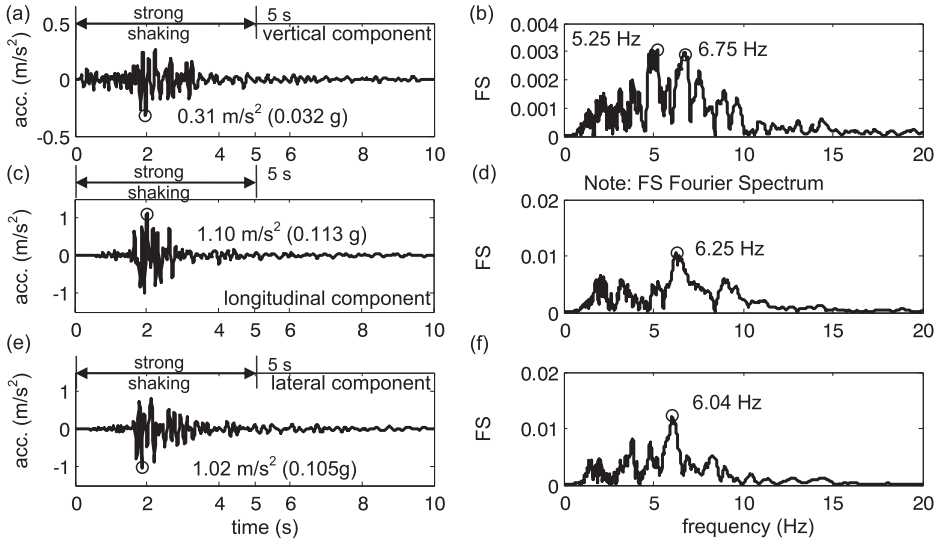

Figure 9. The acceleration time histories (a, c, and e) and pertinent Fourier spectra (b, d, and f) of the three components of the ground motion recorded on July 15, 2012 in Nakagawa Japan, at HKD station.

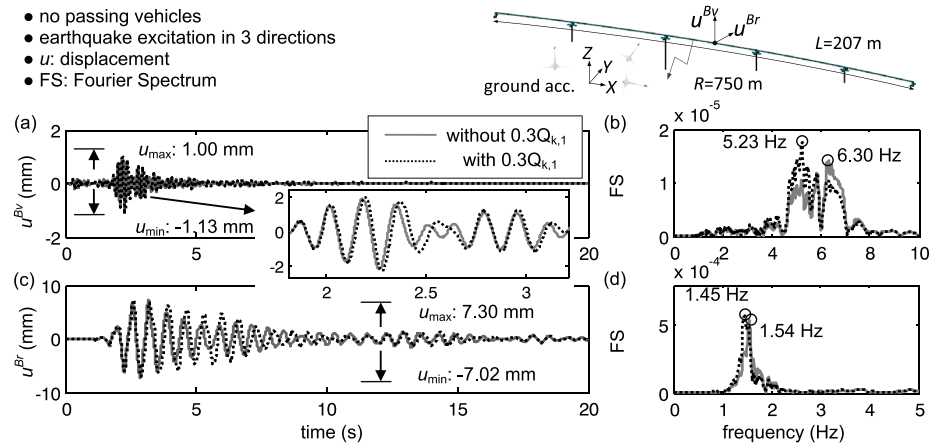

Figure 10. The displacement time histories (a and c) and the pertinent Fourier spectra (b and d) of the response displacements of the midpoint of the bridge for the earthquake excitation of Figure 9. (a) and (b) vertical, (c) and (d) radial degree of freedom. The dynamics of the vehicles are neglected.

stiffness of the piers and the deck, as described in Section 2.1. Figure 10 plots the time histories of the bridge displacement for the earthquake of Figure 9 without considering the vehicle dynamics, together with the pertinent Fourier spectra. The additional mass ($0.3Q_{k,1}$) increases somewhat the natural period of the bridge, and for this particular earthquake (Figure 9), it amplifies the vertical and the radial displacements of the deck (Figure 10(a) and (c)). The predominant frequencies of the Fourier spectra (Figure 10(b) and (d)) correspond to the first transverse and the third vertical eigenmodes of the bridge (Figure 3), as expected. Figure 11 plots the deformed shape of the whole bridge, for the same three time instants as Figure 8. The results of Figure 11 do not account for the additional $0.3Q_{k,1}$ mass; hence, they are comparable with Figure 8. Note the different deformation patterns of the bridge are due to the running vehicles (Figure 8) and due to the seismic loading (Figure 11), accordingly. For the former, the bridge deflects almost statically downwards in the vertical direction and in the sense of the centrifugal forces in the radial direction (Figure 8). The seismic-induced bridge vibration though is of alternating sign (Figure 11) and of higher frequency (Figure 10).

DOI: 10.1002/eqe

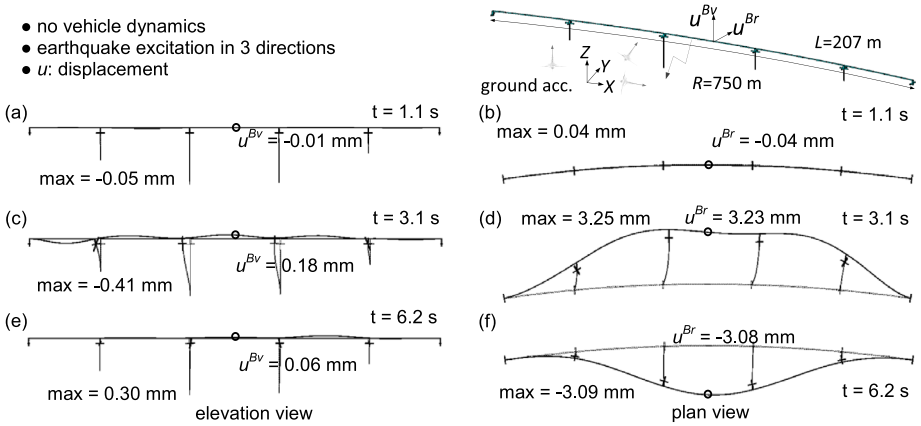

Figure 11. The deformed shape of the whole bridge induced by the earthquake excitation of Figure 9; (a, c, and e) elevation view; (b, d, and f): plan view.

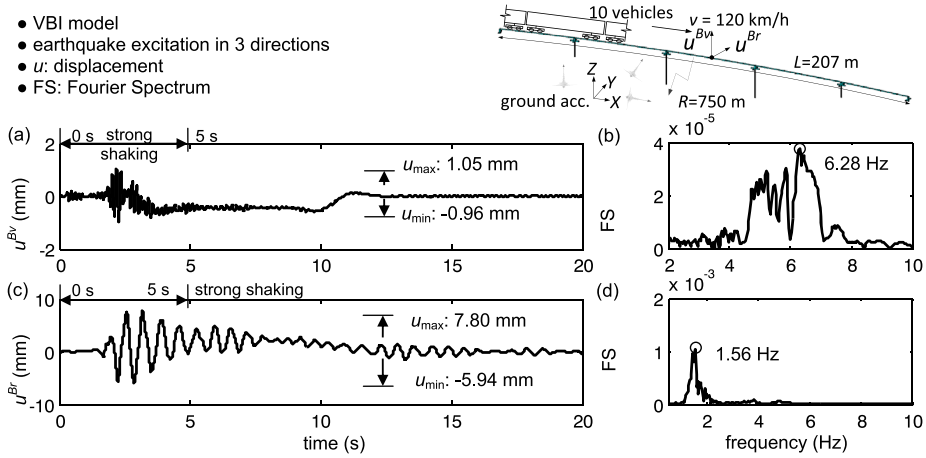

Figure 12. The displacement time histories of the midpoint of the bridge induced by 10 identical moving vehicles and simultaneous earthquake excitation: (a and b) the vertical direction, and (c and d) the radial direction.

3.3. Seismic response analysis of the interacting vehicle–bridge system

Conventional seismic response analysis of bridges focuses on the performance of solely the bridge structure, under mostly strong (rare) earthquake events. In contrast, the scope of the present section is not only to capture the behavior of the bridge but also importantly to examine how the seismic response of the bridge affects the running train vehicles, under moderate (frequent) earthquakes. To this end, the present study proposes the seismic response analysis of the interacting vehicle–bridge system. As a first approach, it is assumed that the earthquake (of Figure 9) strikes when the first vehicle enters the bridge. Later, different time instants the earthquake starts, as well as different sets of earthquake records, are examined. Again, all the analyses in Section 3.3 assume that the effective flexural stiffness of the piers and the effective torsional stiffness of the deck are equal to half the stiffness of the uncrakced sections. The mass of vehicles is modeled directly through the properties of the 3D multibody model (i.e. mass matrix $\mathbf{M}^V$), and hence, no further increase of the mass (e.g. by $0.3Q_{k,1}$) is necessary.

Figure 12 plots the displacement time histories of the bridge along the vertical and the radial senses of the (midpoint of the) deck, together with the pertinent Fourier spectra. Interestingly, the predominant frequencies of the Fourier spectra in Figure 12(b) and (d) are the same as in Figure 10(b) and (d), indicating that the presence of the moving vehicles does not affect significantly the eigenfrequencies of this (particular) bridge. Figure 12 also demonstrates the combined effects of the dynamic VBI (Figure 7)

DOI: 10.1002/eqe

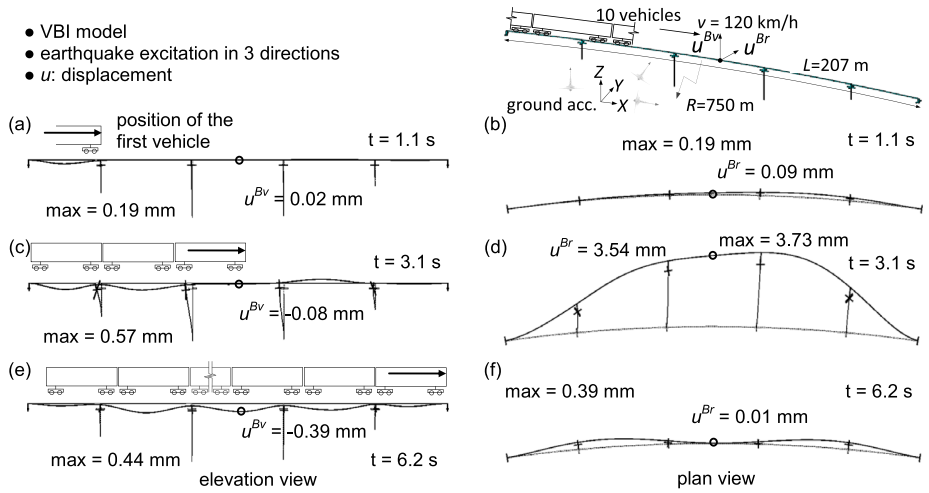

Figure 13. The deformed shape of the whole bridge induced by 10 identical moving vehicles and simultaneous earthquake excitation; (a, c and e) elevation view; (b, d and f) plan view.

and the seismic shaking (Figure 10). Under seismic excitation (Figure 10), the deck vibrates about its unloaded (zero deflection) geometry. However, when the interaction with the vehicles is included in the analysis (Figure 12), the vibration of the deck takes place about its deflected geometry.

Figure 13 displays the deformed shape of the whole bridge, calculated from the proposed seismic response analysis of the interacting vehicle–bridge system. Compare Figures 8, 11, and 13 at, say, $t = 6.2$ s. The vertical displacement from the proposed approach is $u^{Bv} = -0.39$ mm (Figure 13(e)). Similarly, the net vertical deflection due to seismic loading (Figure 11(e)) and due to the running vehicles (Figure 8(e)), accounted for separately, is $u^{Bv} = -0.47 + 0.06 = -0.41$ mm. On the other hand, the radial displacement from the proposed approach is $u^{Br} = 0.01$ mm (Figure 13(f)), which is lower than the net radial deflection $u^{Br} = 2.22 - 3.08$ mm $= -0.86$ mm from Figures 8(f) and 11(f). This difference is attributed to the damping effect the vehicles have on the vibration of the bridge, for example, [12]. This effect is more pronounced in the radial direction than in the vertical direction, where the vibration of the bridge is more intense.

The favorable damping effect the moving vehicles have on the bridge is not a peculiar result of the specific ground motion. For instance, Table I lists the characteristics of a suite of 20 sets of real-ground motions. For all 20 ground motions, Figure 14 compares the 'total' amplitude of the bridge vibration from (i) the proposed seismic analysis of the VBI system; (ii) the seismic analysis of the bridge neglecting the mass and the dynamics of traffic; and (iii) the conventional seismic analysis of the bridge including the mass due to traffic ($0.3Q_{k,1}$). The 'total' amplitude is defined as the absolute sum of the maximum positive and the maximum negative displacements of the midpoint of the bridge ($\left|u^{Bv}_{\max}\right| + \left|u^{Bv}_{\min}\right|$ and $\left|u^{Br}_{\max}\right| + \left|u^{Br}_{\min}\right|$, for example, Figure 12). For simplicity, it is assumed that the earthquake strikes when the first vehicle enters the bridge. The conventional seismic analysis consistently overestimates the response of the bridge, compared with the proposed seismic response analysis, which explicitly simulates the dynamics of the vehicles. This is true, even if the mass due to live loads is not accounted for. This observation verifies the previous conclusions of [2, 11, 12].

Under the same assumptions as Figure 14, Figure 15 summarizes the peak response of the first, the fifth, and the 10th vehicles for the earthquake suite of Table I. The vehicle's peak acceleration, in the radial direction, is beyond the 'comfort' limits of current codes, for example, [32] for more than half of the records examined. Note though that these limits do not refer to earthquake shaking conditions. On the other hand, the derailment factor of the vehicle exceeds, or nears, the pertinent code safety thresholds (e.g. [32]) for earthquake nos. 12, 15, 19, and 20 of Table I. The offload factor exceeds the thresholds for earthquake no. 20. This is more alarming considering that these earthquakes are frequent earthquakes (Mw $\leqslant 6$). Further, Figure 15 reveals that near-fault ground motions (e.g. nos. 11 to 20 of Table I) are more likely to be critical for the safety/stability of the running vehicles. Interestingly, this is not always a factor of the acceleration amplitude. For instance, the peak offload and derailment factors

DOI: 10.1002/eqe

Table I. Properties of the examined earthquakes.

number	name	Station	Mag.	Epic. Dist. (km)	Dur. (s)	X PGA (g)	Y PGA (g)	Z PGA (g)
1	Coyote Lake	CDMG Station 1492	5.74	26.85	26.83	0.07	0.11	0.04
2	Livermore	CDMG Station 67070	5.42	31.54	30.00	0.11	0.05	0.01
3	San Francisco	CDMG Station 1117	5.28	27.03	25.50	0.10	0.11	0.05
4	Trinidad	CDMG Station 1498	5.7	71.24	21.45	0.17	0.13	0.03
5	Jiashi	Xiker, Northwest China	5.8	39.73	40.00	0.14	0.08	0.05
6	Chalfant Valley	CDMG 54100	5.77	27.03	39.97	0.06	0.05	0.03
7	Matata, New Zealand	Edgecumbe substation	5.7	45.76	29.50	0.04	0.04	0.04
8	Yorba Linda	La Harba & Monte Vista	4.27	16.63	43.00	0.03	0.04	0.01
9	Northwest Calif-01	Ferndale City Hall	5.5	43.28	40.00	0.15	0.09	0.03
10	Lytle Creek	Cedar Springs Pumphouse	5.33	22.94	10.22	0.06	0.07	0.04
11	Almiros-01, Greece	Almiros	5.2	14.76	22.59	0.07	0.07	0.07
12	Hollister-04	CDMG 47189	5.45	11.35	80.00	0.04	0.09	0.05
13	Nakagawa	HKD025	4.2	7.00	70.00	0.11	0.10	0.03
14	San Francisco	Golden Gate Park	5.28	11.02	39.72	0.09	0.10	0.03
15	Managua Nicaragua-02	Managua ESSO	5.2	4.33	48.00	0.26	0.22	0.18
16	Oroville-04	Medical Center	4.37	10.50	12.52	0.08	0.05	0.03
17	Oroville-03	DWR Garage	4.7	6.03	13.60	0.11	0.22	0.09
18	Imperial Valley-07	Calexico Fire Station	5.01	13.32	19.42	0.10	0.07	0.03
19	Almiros-02, Greece	Almiros	5.2	13.25	22.60	0.07	0.07	0.09
20	Mammoth Lakes-10	Convict Creek	5.34	6.50	40.00	0.16	0.15	0.10

Data from [39,40]
Mw, magnitude; epic. dis., epicentral distance; Dur, duration.

for records nos. 19 and 20 are comparable, even though the lateral peak ground accelerations (PGAs) of record no. 19 are less than half those of no. 20, and as low as 0.07 g. Clearly, this is an important issue that deserves further research; however, this is a task beyond the scope of the present paper.

Figure 16 shows the acceleration time histories of the car body of the first and the 10th vehicles, for the earthquake of Figure 9. The strong earthquake shaking duration is from 0 to 5 s. Hence, for a $v = 120$ km/h speed and a $L = 207$ m bridge length, the first and the 10th (last) vehicles are running on the deck from 0 to 6.82 s and from 6.75 to 13.58 s, respectively (Figure 16). Recall that the distinct vehicles are dynamically independent. Thus, the vibration of the two vehicles from $t = 0$ to $t = 6.75$ s differs only because of the response of the bridge, which 'filters' the base excitation

DOI: 10.1002/eqe

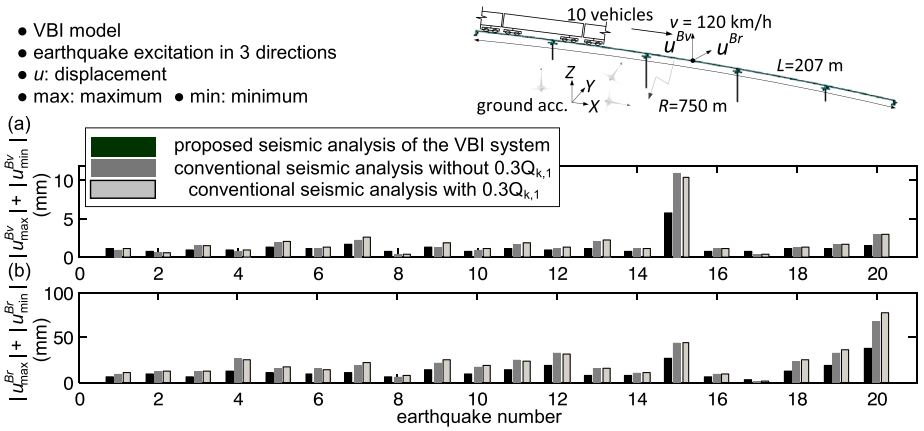

Figure 14. The 'total' vibration amplitude of the midpoint of the bridge under different earthquakes: (a) vertical and (b) radial directions. VBI, vehicle–bridge interaction.

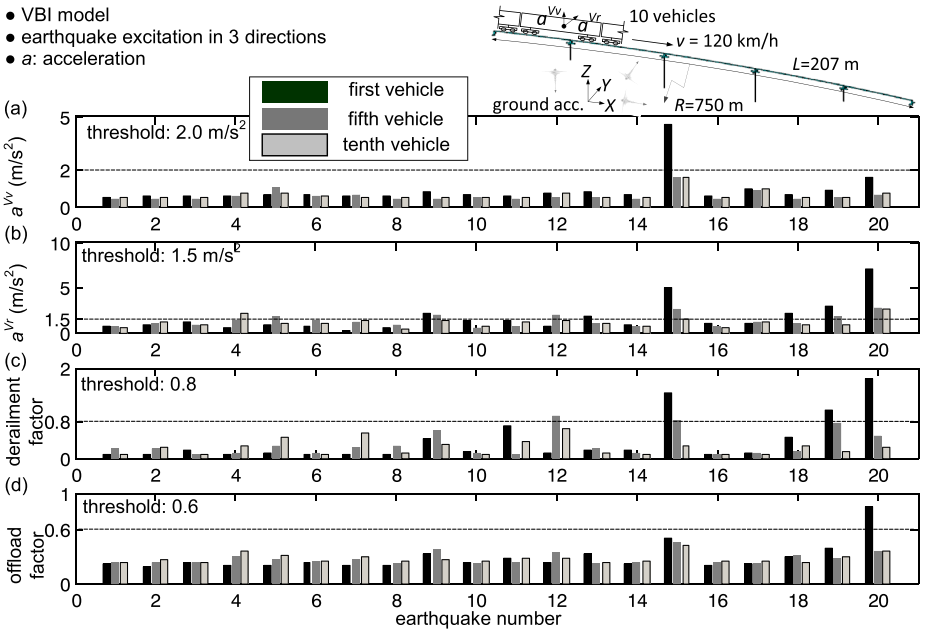

Figure 15. The peak response of the first, the fifth, and the 10th vehicles under different earthquakes: (a and b) the vertical and the radial accelerations of the car body, respectively, (c) the derail factor, and (d) the offload factor.

the first vehicle experiences. The acceleration of the first vehicle running on the bridge (Figure 16(a) and (c)) is amplified (in this case doubled) compared with that of the 10th vehicle, which is still running on the ground (Figure 16(b) and (d)). By the time the 10th vehicle is running on the bridge, the earthquake has decayed, and the vibration of the bridge resembles more free vibration (Figure 12). Consequently, the amplification of the acceleration of the 10th vehicle, while still visible in the radial direction between 6.75 and 13.58 s (Figure 16(d)), is lower than that (of the first vehicle) during the strong ground shaking between 0 and 5 s. Figure 16(e) and (f) plots the pertinent normal contact force $\lambda_N{}^{(2)}$ and lateral creep force $\lambda_{Ty}{}^{(2)}$ of the second (inner) wheel (Figure 6) of the first vehicle. For the examined excitations, the seismic vibration of the bridge affects more the lateral creep force than the normal contact force (Figure 16(e) and (f)). In summary, the seismic response of the bridge (examined) has an adverse influence on the passing vehicles. The spectral amplification of the response of the vehicle due to the excited bridge depends also on the position of the running vehicle on the deck during the strong earthquake shaking. It is therefore an inherently 'timing' problem.

DOI: 10.1002/eqe

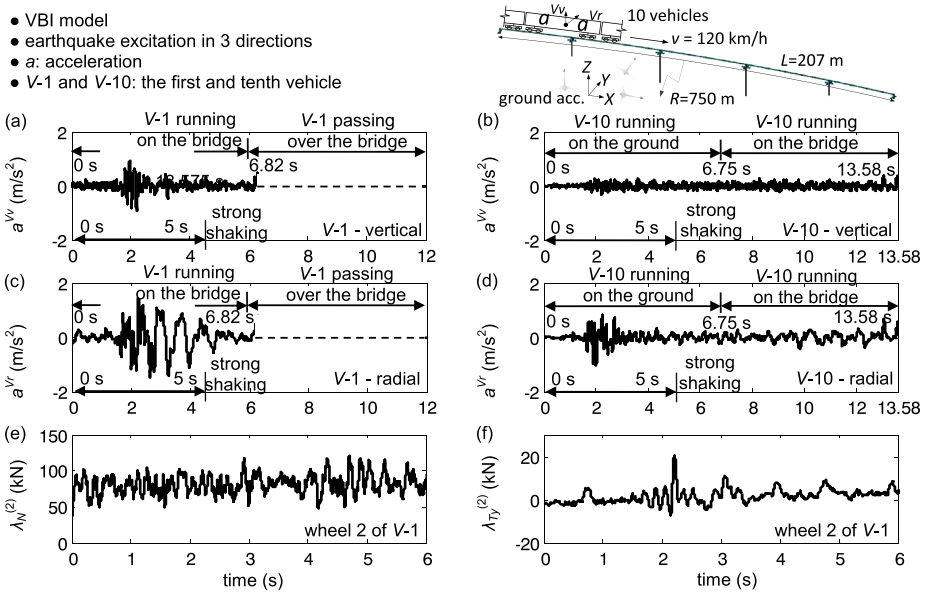

Figure 16. The car-body acceleration time histories of (a and c) the first vehicle and (b and d) the 10th/last vehicle induced by 10 identical vehicles and simultaneous earthquake excitation: (a and b) the vertical direction; (c and d) the radial direction; (e and f) the normal contact force and the lateral creep force of the second wheel of the first vehicle. VBI, vehicle–bridge interaction.

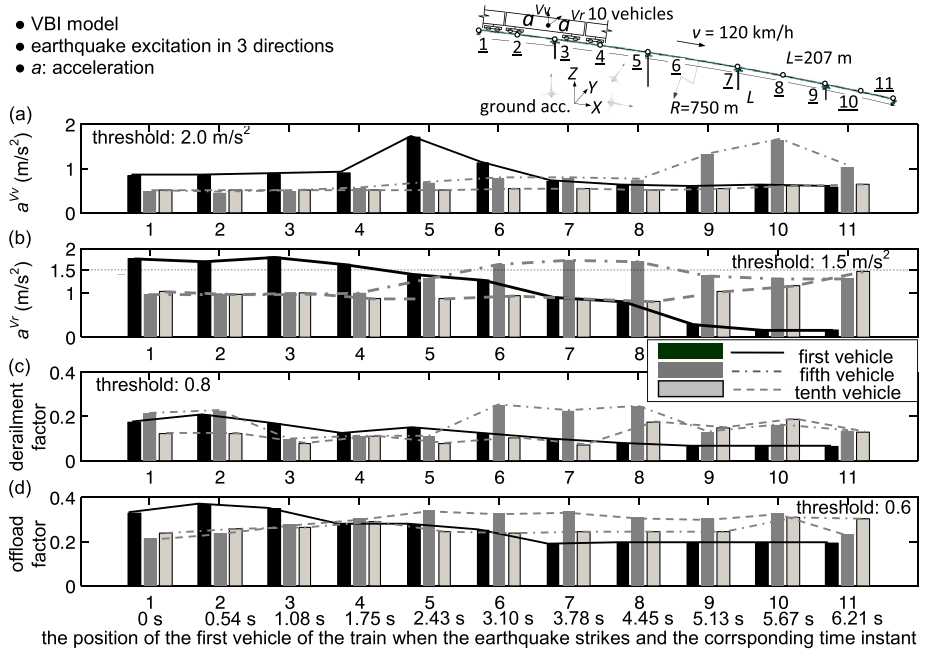

Figure 17. The peak response of three vehicles, considering different time instants the earthquake occurs: (a and b) the vertical and the radial peak accelerations, respectively, (c) the peak derailment, and (d) the offload factor. VBI, vehicle–bridge interaction.

The position of a running vehicle on a bridge shaken by earthquake excitation is unpredictable. To shed light on the vehicle–bridge–earthquake 'timing' problem, Figure 17 examines 11 different positions of the train on the deck when the earthquake commences. These 11 positions correspond to the first vehicle being at either the midpoints of the five spans or over the six piers/abutments of the bridge. The response analysis starts at $t = 0$ s when the first vehicle enters the bridge, but the

DOI: 10.1002/eqe

earthquake excitation (of Figure 9) strikes when the first vehicle of the train reaches one of the 11 positions (the corresponding time is also shown in Figure 17). Figure 17 plots the peak values of the critical metrics for the riding comfort and the safety of the vehicles. The continuous lines connect the peaks of the three vehicles for the 11 positions to highlight the general trend. The response of the first vehicles is higher when the earthquake strikes earlier (Figure 17), while the response of the succeeding vehicles (fifth and 10th vehicles) is higher when the earthquake strikes later (Figure 17). In other words, as a rule of thumb, the response of the vehicles amplifies, when the strong ground motion shaking finds them running on the bridge. As an order of magnitude, the amplification of the acceleration of a vehicle, due to the seismic response of the bridge, can reach values of 3 or higher, while the amplification of the safety metrics (offload and derailment factors) is in the order of 2. In summary, the seismic response of the bridge has a significant, adverse effect on the safety of the vehicle, and given the stochastic nature of earthquakes, the problem beckons for a probabilistic treatment.

4. CONCLUSIONS

This study examines the seismic response of an interacting vehicle–bridge system under frequent earthquakes. In view of the recent developments in railway transportation and the pertinent accidents reported already, this is a problem of increasing importance. The proposed response analysis simulates the 3D dynamics of the moving vehicles and uses a complete, 3D finite element model of the bridge. The paper focuses on a horizontally curved railway bridge and train vehicles crossing the bridge during different times periods of the ground motion excitation.

For the particular (vehicle–bridge) case studied, frequent earthquakes, of moderate amplitude, do not pose a threat for the integrity of the bridge. The analysis even confirms that the running vehicles might have a favorable damping effect on the vibration of the deck. However, the seismic response of the bridge reduces the safety of the vehicles running on it compared with same vehicles running on the ground during the same excitation. Even for a given vehicle–bridge case, the extent of this reduction is a complicated multi-parametric problem. It depends not only on, including but not limited to, the intensity, the frequency, and the kinematic characteristics (e.g. near fault or far field) of the earthquake record but also on a vehicle–bridge–earthquake timing problem. More specifically, the particular position of the running vehicles on the deck, when the earthquake occurs, affects significantly the response/safety of the vehicle. The results show that under most of the moderate earthquakes examined, the riding comfort of the vehicles exceeds, as expected, the pertinent contemporary code requirements. More alarming finding though is that even frequent earthquakes, of moderate intensity, can threaten the safety of the vehicles running on the bridge during the ground motion excitation. Finally, while the present study offers a glimpse into the salient features of the vehicle–bridge–earthquake coupling, this is an important but complicated problem, which deserves further research. Thus, the paper also pinpoints directions for future research related to the influence of the particular kinematic characteristics of the seismic ground motion on the response of vehicle–bridge system as well as to a probabilistic treatment of the vehicle–bridge–earthquake timing problem.

REFERENCES

1. Guo WW, Xia H, Roeck DG, Liu K. Integral model for train-track-bridge interaction on the sesia viaduct: dynamic simulation and critical assessment. *Computers & Structures* 2012; **112**:205–216.
2. Kim C W, Kawatani M, Lee CH, Nishimura N. Seismic response of a monorail bridge incorporating train-bridge interaction. *Structural Engineering and Mechanics* 2007; **26**(2):111–126.
3. Xia H, Han Y, Zhang N, Guo WW. Dynamic analysis of train-bridge system subjected to non-uniform seismic excitations. *Earthquake Engineering & Structural Dynamics* 2006; **35**(12):1563–1579.
4. Ju SH. Nonlinear analysis of high-speed trains moving on bridges during earthquakes. *Nonlinear Dynamics* 2012; **69**(1-2):173–183.
5. Japan web: earthquake warning-stop that bullet train. (Available from: http://web-japan.org/nipponia/nipponia33/en/feature/feature10.html) accessed on [15 June 2005].
6. The China post: HSR service south of Taichung to resume. (Available from: http://www.chinapost.com.tw/taiwan/national/national-news/2010/03/05/246940/HSR-service.htm) accessed on [5 March 2010].
7. Kappos AJ, Saiidi MS, Aydinoglu MN, Isakovic T. Seismic design and assessment of bridges: inelastic methods of analysis and case studies. *Geotechnical, Geological and Earthquake Engineering* 2012; **21**:1–221.

DOI: 10.1002/eqe

8. Priestley MJN, Seible F, Calvi GM. *Seismic Design and Retrofit of Bridge*, John Wiley & Sons: New York, 1996.
9. Dimitrakopoulos EG, Zeng Q. A three-dimensional dynamic analysis scheme for the interaction between trains and curved railway bridges. *Computers & Structures* 2015; **149**:43–60.
10. Yang YB, Wu YS. Dynamic stability of trains moving over bridges shaken by earthquakes. *Journal of Sound and Vibration* 2002; **258**(1):65–94.
11. Kim CW, Kawatani M. Effect of train dynamics on seismic response of steel monorail bridges under moderate ground motion. *Earthquake Engineering & Structural Dynamics* 2006; **35**(10):1225–1245.
12. Kim CW, Kawatani M, Konaka S, Kitaura R. Seismic responses of a highway viaduct considering vehicles of design live load as dynamic system during moderate earthquakes. *Structure and Infrastructure Engineering* 2011; **7**(7-8):523–534.
13. Design specification of highway bridges. Part V Seismic design. *Japan Road Association*, Tokyo: Japan, 2002.
14. He X, Kawatani M, Hayashikawa T, Matsumoto T. Numerical analysis on seismic response of Shinkansen bridge–train interaction system under moderate earthquakes. *Earthquake Engineering and Engineering Vibration* 2011; **10**(1):85–97.
15. Tanabe M, Matsumoto N, Tanabe Y, Wakui H, Sogabe M, Okuda H. A simple and efficient numerical method for dynamic interaction analysis of a high-speed train and railway structure during an earthquake. *Journal of Computational and Nonlinear Dynamics* 2008; **3**(4):041002.
16. Tanabe M, Matsumoto N, Wakui H, Sogabe M. Simulation of a Shinkansen train on the railway structure during an earthquake. *Japan journal of industrial and applied mathematics* 2011; **28**(1):223–236.
17. Tanabe M, Wakui H, Sogabe M, Matsumoto N, Tanabe Y. An efficient numerical model for dynamic interaction of high speed train and railway structure including post-derailment during an earthquake, *8th International Conference on Structural Dynamics*: EURODYN, Leuven, Belgium, 2011; 1217–1223.
18. Matsumoto N, Sogabe M, Wakui H, Tanabe M. Running safety analysis of vehicles on structures subjected to earthquake motion. *Quarterly Report of RTRI* 2004; **45**(3):116–122.
19. Du XT, Xu YL, Xia H. Dynamic interaction of bridge-train system under non-uniform seismic ground motion. *Earthquake Engineering & Structural Dynamics* 2012; **41**(1):139–157.
20. Yau JD, Fryba L. Response of suspended beams due to moving loads and vertical seismic ground excitations. *Engineering Structures* 2007; **29**(12):3255–3262.
21. Fryba L, Yau JD. Suspended bridges subjected to moving loads and support motions due to earthquake. *Journal of Sound and Vibration* 2009; **319**(1):218–227.
22. Yau JD. Interaction response of maglev masses moving on a suspended beam shaken by horizontal ground motion. *Journal of Sound and Vibration* 2010; **329**(2):171–188.
23. Zhang ZC, Lin JH, Zhang YH, Zhao Y, Howson WP, Williams FW. Non-stationary random vibration analysis for train-bridge systems subjected to horizontal earthquakes. *Engineering Structures* 2010; **32**(11):3571–3582.
24. Montenegro PA, Calçada R, Vila Pouca N, Tanabe M. Running safety assessment of trains moving over bridges subjected to moderate earthquakes, *Earthquake Engineering & Structural Dynamics*, 2015. DOI: 10.1002/eqe.2673.
25. Montenegro PA, Neves SGM, Calçada R, Tanabe M, Sogabe M. Wheel-rail contact method for analyzing the lateral train-structure dynamic interaction. *Computers and Structures* 2015; **152**:200–214.
26. Zhang N, Xia H, Guo WW. Vehicle-bridge interaction analysis under high-speed trains. *Journal of Sound and Vibration* 2008; **309**(3):407–425.
27. EN 1998-2. Eurocode 8. *Design of Structures for Earthquake Resistance-Part 2: Bridges*, European Committee for Standardization (CEN): Brussels, 2005.
28. Yang YB, Wu YS, Yao ZD. *Vehicle-bridge Interaction Dynamics: With Applications to High-speed Railways*, World Scientific: Singapore, 2004.
29. ANSYS. *ANSYS User's Manual Version 14.0.*, ANSYS Inc.: Houston, USA, 2011.
30. MathWorks. *MATLAB User's Guide*, The MathWorks Inc: Natick, MA, 1994–2013.
31. Seokho J. *Response Analysis of a Seismic Isolated Railway Bridge under Service and Earthquake Loading*, University of Patras: Master Thesis, 2008.
32. Xia He and Roeck G and Goicolea JM. *Bridge Vibration and Controls: New Research*, Nova Science Publisher's: New York, 2012.
33. Shabana AA, Zaazaa KE, Sugiyama H. *Railroad Vehicle Dynamics: A Computational Approach*, CRC Press: New York, 2010.
34. Antolin P, Zhang N, Goicoleaa JM, Xia H, Astiza MA, Olivaa J. Consideration of nonlinear wheel-rail contact forces for dynamic vehicle-bridge interaction in high-speed railways. *Journal of Sound and Vibration* 2013; **332**: 1231–1251.
35. Pfeiffer F. *Multibody Dynamics with Unilateral Contacts*, Vol. 9, John Wiley and Sons: Singapore, 1996.
36. Shen ZY, Hedrick JK, Elkins JA. A comparison of alternative creep force models for rail vehicle dynamic analysis. *Vehicle System Dynamics* 1983; **12**(1-3):79–83.
37. Lee SY, Cheng YC. Nonlinear analysis on hunting stability for high-speed railway vehicle trucks on curved tracks. *Journal of vibration and acoustics* 2005; **127**(4):324–332.
38. Shampine LF, Mark WR. The MATLAB ODE suite. *SIAM journal on scientific computing* 1997; **18**(1):1–22.
39. Earth Science and Disaster Prevention (NIED). (Available from: http://www.kyoshin.bosai.go.jp/kyoshin/docs/overview_kyoshin_en.shtml) accessed on [29 January 2015].
40. PEER Ground Motion Database Pacific Earthquake Engineering Research Center. (Available from: http://ngawest2.berkeley.edu/site) accessed on [4 May 2015].

DOI: 10.1002/eqe